Reduction and Reconstruction of Co_3O_4 Nanocubes upon Carbon Deposition

Ji Feng and Hua Chun Zeng*

Department of Chemical and Biomolecular Engineering, Faculty of Engineering, National University of Singapore, 10 Kent Ridge Crescent, Singapore 119260

Received: May 15, 2005; In Final Form: July 2, 2005

We describe a synthetic investigation on the formation of carbon nanofibers using a preshaped free-standing metal-oxide catalyst (single-crystal cobalt oxide (Co_3O_4) nanocubes). In reacting with acetylene (C_2H_2) vapor, Co_3O_4 nanocubes are reduced and reconstructed into metallic cobalt. The resultant metal catalyst with a 2-fold symmetry leads to a bilateral base growth for carbon nanofibers. Our findings indicate that an understanding of catalyst-assisted chemical vapor deposition (CVD) mechanisms can be acquired, when the shape, size, and crystal orientation of pristine metal catalysts are made known to the CVD process. By tracing their evolutional changes in structure and composition, the shape-designed model catalysts may offer new opportunities for mechanistic investigations on the chemical reactivity of nanoparticles, general catalyst-assisted material synthesis, and metal intercalation chemistry.

Introduction

The past decade has witnessed an explosive increase in nanomaterial research, triggered by the discovery of carbon nanotubes (CNTs) in 1991.[1] The graphene layers in CNTs are parallel to the axis of the nanotube, which is different from the cone-shaped carbon nanotubes known much earlier.[2] Among various studies on novel nanostructured materials, investigation on CNTs is still taking the lead owing to their unique structural, electronic, and mechanical properties.[1−5] There have been a number of mechanisms,[6−18] often in controversy, to describe the nucleation and growth of carbon nanotubes/filaments/fibers under catalytic chemical vapor deposition (CVD) conditions. However, the geometrical structures and shapes of initial catalysts used in many of these works were not defined and quantified, which caused additional uncertainty for the mechanisms classified. Among many proposed mechanisms,[6−18] two basic modes are attributed: (i) base growth[6−9] and (ii) tip growth.[12−15] During the "base growth", catalyst particles essentially remain on the supporting substrate while CNTs grow rising up from the catalyst base. In the "tip growth", on the other hand, catalyst particles are lifted off from the substrate support, staying at the tip of the CNTs which are formed like traces behind the catalyst particles. It has been conceived that the two growth modes may bare some similarity in terms of carbon diffusion/insertion on the metal catalyst surface. In both cases, for example, the nanocarbons are grown only at one side of the catalyst particles; that is, they are grown unilaterally. In addition to these *unilateral* growths,[12−15] nanocarbons can also grow *bilaterally* at two opposite sides of metal particles, resulting in metal inclusions in the nanocarbons.[2,10,11] In all of these cases, metal inclusions in either cylindrical graphene CNTs,[12−15] cone-shaped carbon bi-tubes,[2] or flat graphitic planar stacks and fibers[10,11] were actually dug out of the surface of catalytic metal/alloy supports. Because the primitive forms of metal particles before this "digging" are not known, process history cannot be traced and related growth modes cannot be assigned unambiguously. Very recently, the metal-inclusion process in the *unilateral* growth of CNTs was demonstrated successfully with in situ high-resolution transmission electron microscopy (HRTEM) observation.[13] In this connection, we notice that the metal-inclusion mechanism in the *bilateral* growth of nanocarbons could be further pursued by taking advantage of the synthetic architecture of transition metal oxides.[19−25] Herein, we describe an investigation on the formation mechanism of carbon nanofibers (i.e., bi-cone-shaped CNTs) with a preshaped free-standing model catalyst (Co_3O_4 nanocubes) concerning metal-oxide reduction, reconstruction, and metal−carbon interactions under CVD conditions. Our findings indicate that using shape-defined nanocatalysts may provide new opportunities for mechanistic investigations on the chemical reactivity of nanoparticles, general catalyst-assisted material synthesis, and metal intercalation chemistry.

Experimental Section

The preshaped catalyst, nanocubic Co_3O_4 (in the spinel phase), was prepared via a salt-assisted oxidation method detailed in our previous studies.[19,20] Briefly, 1.2 g of NaOH (Merck, >99.0%) was dissolved in 100.0 mL of deionized water in a three-necked round-bottom flask, after which 120.0 g of $NaNO_3$ (Merck, >99.5%) was added. The three-necked flask, mounted on top with a reflux condenser, was then immersed into an oil bath at 105 ± 0.2 °C. A purified air stream (50 mL/min, Soxal, O_2 = 21 ± 1%, H_2O < 2 vpm and hydrocarbons < 5 vpm; vpm = volume per million) was continuously bubbled through this solution. After 30 min, 20.0 mL of 1.0 M $Co(NO_3)\cdot 6H_2O$ (Merck, >99.0%) was added dropwise within 1 min under stirring, and a blue precipitate (α-$Co(OH)_2$) was formed instantaneously. The blue slurry was kept in the oil bath for further reactions with the same air stream. After the reactions, the slurry was cooled naturally under ambient conditions to room temperature and centrifuged at 3000 rpm for 20 min. The obtained solid was redispersed in a HCl solution in order to dissolve the unconverted solid precursors such as $Co(OH)_2$, $Co^{II}(OH)_{2-x}(NO_3)_x\cdot mH_2O$, and $Co^{II,III}$-hydrotalcite.[19,20] The mixture was centrifuged again, and the process was repeated four times to ensure a complete removal of the precursor phases.

* Corresponding author. E-mail: chezhc@nus.edu.sg.

10.1021/jp052551n CCC: $30.25
Published on Web 08/23/2005

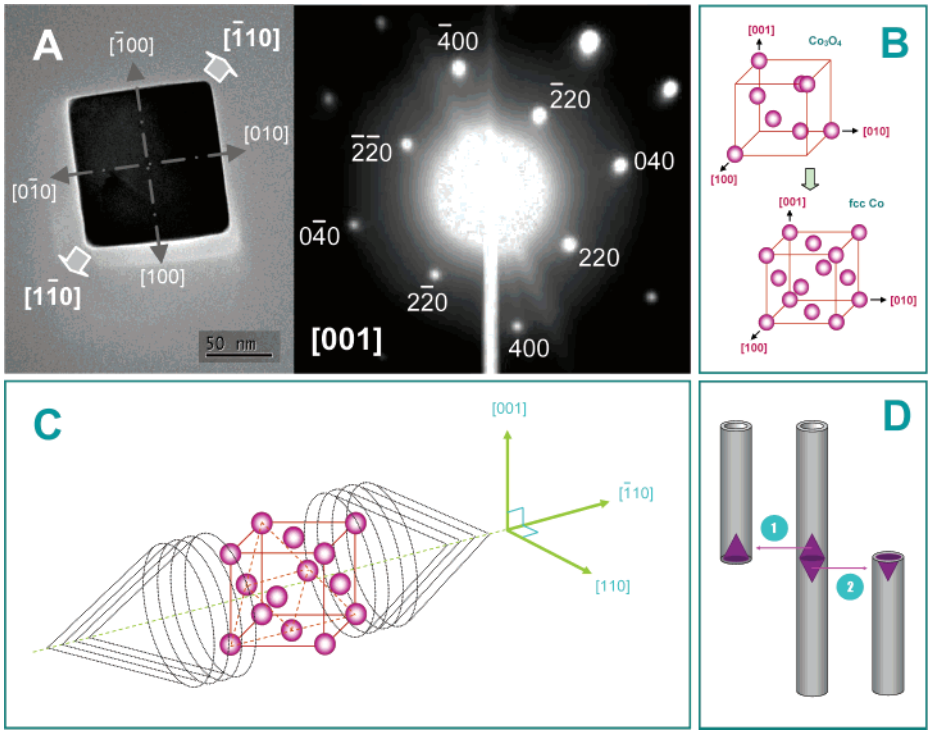

Figure 1. (A) TEM image of an as-prepared Co_3O_4 nanocube and its SAED pattern (the large, wide arrows indicate the lateral elongation directions upon the C_2H_2-CVD process). (B) A simplified representation of one-eighth of a unit cell of Co_3O_4 spinel (cobalt cations are illustrated with purple balls; oxygen anions are not shown) and a unit cell of fcc Co metal (cobalt atoms are depicted with purple balls). (C) Orientation of metallic Co and the formation of conical-shaped carbon nanofibers along the ⟨110⟩ directions of cobalt. (D) Bilateral base growth mechanism with a symmetric Co catalyst for carbon nanotubules: (1) upper base mode; (2) lower base mode.

A black paste product (i.e., Co_3O_4 nanocubes in 100% morphological yield) was then resuspended in deionized water and recentrifuged; this latter washing procedure was also repeated four times. Chemical vapor deposition (CVD) synthesis of metal−carbon-nanofiber composites was carried out in a horizontal quartz-tube reactor (inner diameter of 7 mm) with acetylene (C_2H_2) diluted by purified argon gas. The cubic nanocatalyst Co_3O_4 was supported on glass wool and pressed into a small packed bed. The catalyst was preheated in an electric furnace to 400−500 °C at 10 °C/min and purged with an argon stream. In most cases, the argon was fed as a background gas at a constant feed rate of 40 mL/min, and the carbon source gas acetylene was introduced at a variable rate of 5−10 mL/min when the temperature reached a desired value. This CVD process was kept going for 3−20 min, and then, the C_2H_2 stream was shut down. The reactor was moved out of the heating zone of the furnace and brought down to room temperature naturally with the same flow of argon. The black powder product was then stored in clean glass bottles for further material characterization. In particular, the crystal phase was determined with powder X-ray diffraction (XRD, Shimadzu XRD-6000, Cu Kα radiation). The structural and compositional information of the product materials were obtained with transmission electron microscopy and selected area electron diffraction (TEM/SAED, JEM-2010F, 200 kV), high-resolution TEM and energy-dispersive X-ray spectroscopy (HRTEM/EDX, JEM-300, 300 kV), and X-ray photoelectron spectroscopy (XPS, AXIS-HSi, Kratos Analytical).

Results and Discussion

A representative Co_3O_4 nanocube prepared from the above procedure is shown in Figure 1A. In the present synthesis, the mean length of cube edges was controlled at 86 ± 6 nm (Supporting Information SI-1). On the basis of our selected area electron diffraction (SAED) and TEM-tilting experiments (Supporting Information SI-1), it is known that each nanocube is bordered with six crystallographic planes of {100} (Co_3O_4; space group *Fdιm*; a_o = 8.084 Å, JCPDS file no. 43-1003). In this work, the conversion of the Co_3O_4 nanocubes to metallic Co was carried out in a flowing stream of acetylene (C_2H_2) upon the graphitization of the organic molecules (Figure 1B and C). Considering the isotropic nature of the prepared Co_3O_4, a number of scenarios for carbon deposition can be proposed: (i) on 6 equal crystal planes; (ii) at 8 equal corners; and (iii) on 12 equal edges of a cubic structure. Quite surprisingly, the experimental results reveal that due to self-induced growth anisotropy only one-dimensional carbon deposition proceeds, as depicted in Figure 1C and D.

The specific volumes of atomic cobalt for Co_3O_4 and Co are 14.68 and 11.22 Å^3/atom, respectively. Because the volume shrinkage from Co_3O_4 to Co is only moderate and similar crystal symmetry is maintained, it is expected that the resultant Co crystallites would preserve the original cubic shape of Co_3O_4 upon the volume contraction. Figure 2 displays a few representative TEM images of cobalt-containing carbon nanofibers grown in the above process, each with a black nodule (cobalt catalyst) in the middle. Indeed, some of the cobalt centers are still cubelike, as shown in Figure 3A, although the majority shows an elongated morphology (Figure 2A−C). The energy-dispersive X-ray analysis (EDX) affirms that cobalt and carbon are present in these nanofibers (Supporting Information SI-2). In this agreement, SAED investigation (Figure 2B and C) further confirms that all of the Co_3O_4 nanocubes have been transformed to metallic cobalt and the included cobalt nanoparticles are single-crystalline. On the basis of observed diffraction spots of the [110] and [111] zones, it is revealed unambiguously that all resultant bi-cone-shaped cobalt nodules are elongated along the ⟨110⟩ directions, which is in good agreement with an

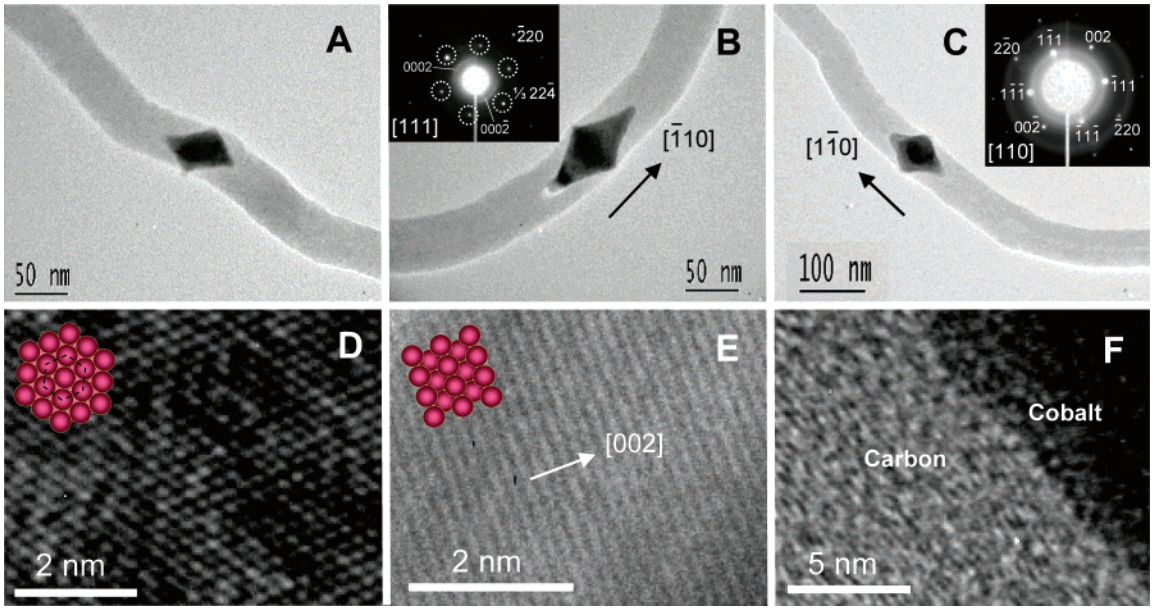

Figure 2. (A−C) TEM images of carbon nanotubules formed with rhombic cobalt catalysts (converted from Co_3O_4 nanocubes) in the center and their respective SAED patterns of [111] and [110] zone spots (insets). (D) Lattice-resolved HRTEM image perpendicular to {111} planes (illustrated with a colored model of the (111) surface; a surface unit cell of $3 \times \{422\}$ is indicated with a dashed hexagon). (E) HRTEM image of d_{002} lattice fringes (illustrated with a colored model of the (110) surface). (F) HRTEM image on the interfacial area between a conical Co crystal tip and grown graphene layers surrounding it.

investigation on the formation of metallic bi-cones and their related carbon bi-tubes.[2] The high crystallinity of single-crystal cobalt inclusions is also elucidated in our lattice-resolved HRTEM images. For example, a 6-fold symmetry corresponding to a coplanar atomic arrangement of {111} crystal planes of face-centered cubic (fcc) cobalt can be observed in Figure 2D; the interatomic distance is measured at 2.51 ± 0.02 Å (space group *Fmm*; $a_o = 3.554$ Å; JCPDS card no. 01-1259). It is not surprising to observe $^1/_3\{422\}$ forbidden reflections in the [111] zone spots, since structural defects such as stacking faults[26] along the [111] axis are anticipated for our conversion process of Co_3O_4 to fcc Co. Furthermore, the lattice fringes of d_{002} (1.78 ± 0.03 Å) shown in Figure 2E are in clear association with the ⟨110⟩ orientations of the cobalt. Figure 2F also displays the interfacial structure between the cobalt catalyst and carbon nanofiber, showing the formation of woven graphene layers (average interlayer distance ≈0.34 nm) parallel to the biconical cobalt growth fronts. However, the graphene layers become more parallel to the fiber axis when they are farther away from the catalyst, as shown in Figure 3. Together with those of Figure 2A−C, Figure 4 indicates that the orientation of the cobalt catalyst is along the ⟨110⟩ directions of fcc cobalt exclusively for all linear metal−carbon-nanofiber nanocomposites. The droplet of cobalt confirms that the carbon deposition takes place along the largest diameter part of cobalt catalyst; the growth action also pushes the tip cobalt droplet away from the original catalyst. Consistent with this biconical carbon insertion, two "diffraction arcs" of graphene layers, 0002 and 000−2, are observed in the SAED pattern of Figure 2B. The arc curves in fact comprise numerous diffraction spots, registering different orientations of the graphene layers with respect to the axis of a nanofiber. The carbon nanofibers were grown bilaterally from both sides of a central cobalt (Figure 1C), showing a 2-fold symmetry for the overall composite structure. Because the symmetric Co crystallite was a catalytic substrate tailor-made in our carbon deposition, remarkably, the unique final product morphology reveals a *bilateral* base-mode mechanism (Figure 1D). In principle, on the basis of the current findings, more complex branching (such as *trilateral*) from the central metal should also be attainable when multiple pods of metallic catalysts are synthesized.

The carbon nanofibers synthesized with this approach could be as long as a few micrometers but usually are a few hundred nanometers in length. Image statistics of over 300 cobalt-containing carbon nanofibers shows that only less than 3% of them have diameters greater than 200 nm, and a distribution profile of the nanofibers with diameters smaller than 200 nm is displayed in Figure 5A. It can be seen that, despite the long tail toward the right side, diameters of more than two-thirds of nanofibers fall between 30 and 70 nanometers (Supporting Information SI-3). Hence, a direct link between the Co_3O_4 nanocubes and resultant Co in size, dimension, and crystal orientation is exhibited with respect to both the volume shrinkage and the ⟨110⟩ elongation. More importantly, this observation reveals that a critical size exists for Co_3O_4 nanocubes to undergo the initial graphitization under a set of experimental parameters (see also Figure 8F). The diameter of the nanofiber is proportional to the dimension of the largest cross section of cobalt particle, consistent with an observation involving the surface diffusion of carbon on the active atomic steps,[13] noting that many atomic steps exist on the reshaping biconical cobalt catalyst for this diffusive growth of graphene layers.

The above C_2H_2-CVD process was also investigated with the XRD method (Figure 5B). The diffraction pattern of the sample obtained after 3 min of reaction indicates the formation of a carbon phase, with a reflection at around $2\theta = 26.3°$ (i.e., inter-graphene-sheet distance 3.35 Å). The broad asymmetric peak observed also reveals that the carbon phase was not well integrated. It is also indicative that the precursor spinel oxide had been completely converted to fcc elemental cobalt even within the first 3 min of reaction. Though the lattice of metallic cobalt commonly adopts the hexagonal close-packed (hcp) structure, it has been reported that the fcc packing is a common lattice configuration for nanostructured cobalt.[27] On the basis of the above observations, it is clear that the pristine Co_3O_4 nanocubes were reduced to metallic cobalt while the hydrocarbon feedstock C_2H_2 was oxidized and decomposed into graphene

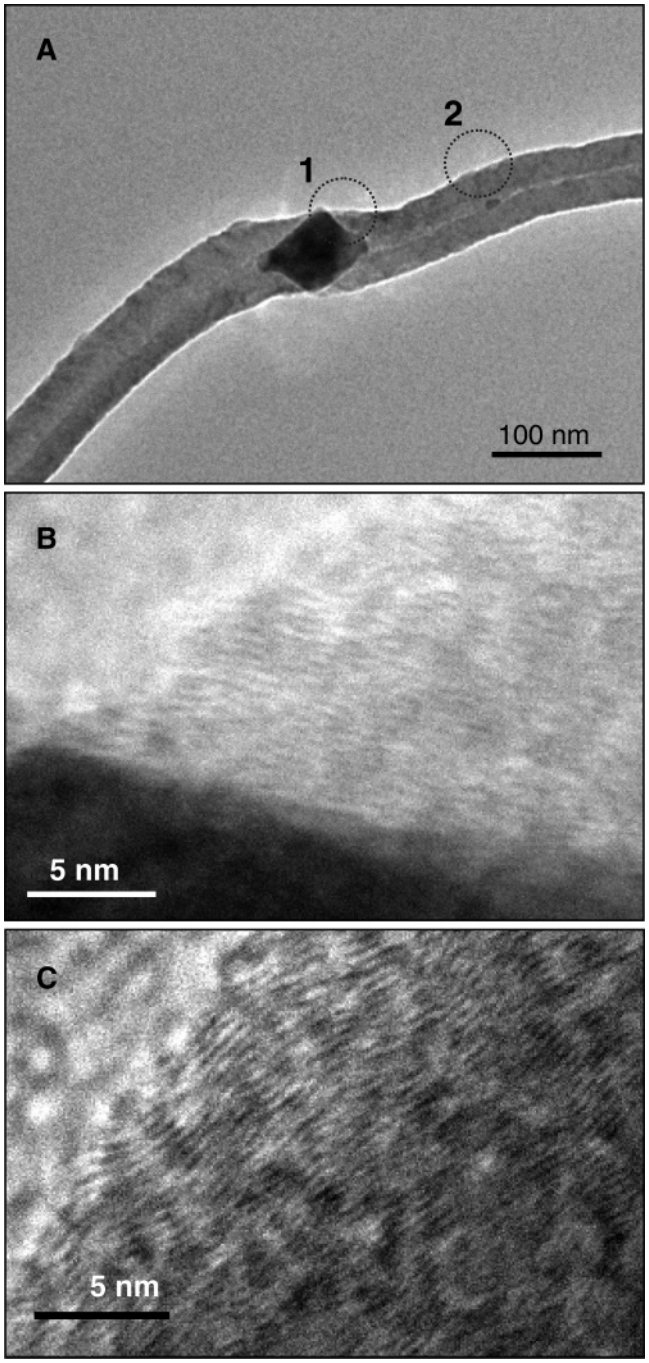

Figure 3. TEM images of Co-containing carbon nanotubules: (A) overall structure; (B) area 1 of part A; (C) area 2 of part A.

carbon. This redox reaction is also verified by an observation of the generation of colorless transparent condensate (H_2O) on the downstream side of the quartz-tube reactor, as explained in the chemical equation

$$Co_3O_4(s) + 4C_2H_2(g) = 3Co(s, fcc) + 8C(s, graphene) + 4H_2O(g) \quad (1)$$

The XRD pattern of the sample obtained after 10 min of reaction provides similar findings, except for the peak narrowing and stronger reflections. In contrast to the pronounced XRD peaks of metallic cobalt observed in the sample after 10 min of CVD treatment, the X-ray photoelectron spectroscopy (XPS) study indicates a very weak signal for the existence of surface cobalt. According to the species present in this system, the elements

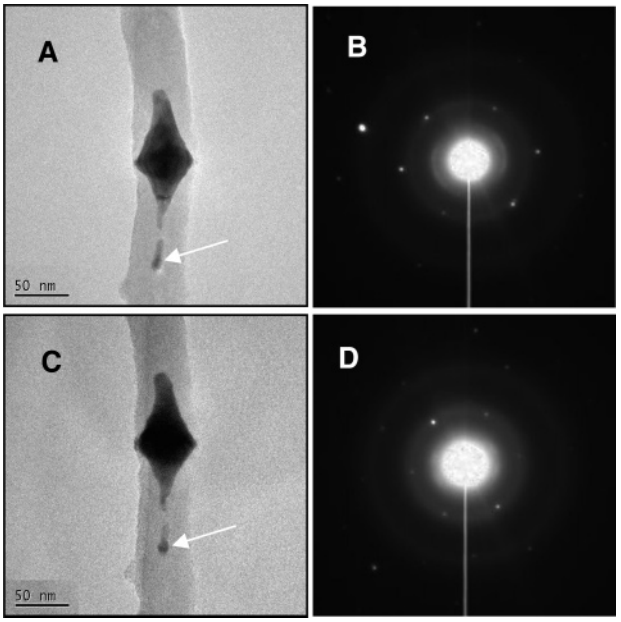

Figure 4. TEM images and SAED patterns of Co-containing carbon nanotubules at different tilted angles: (A) tilted angle 0°; (B) [110] zone diffraction spots from part A (refer to Figure 2C); (C) tilted angle +30°; (D) [111] zone diffraction spots of part C (refer to Figure 2B). The white arrows indicate the cobalt droplets.

detected should be carbon, oxygen, and cobalt. Apart from the wide-scan spectrum reported in Figure 6A, a narrow-scan X-ray photoelectron spectroscopy analysis on the binding energies of core-level photoelectrons C 1s, O 1s, and Co 2p can be found in Figure 6B−D.[28−30] The XPS spectrum shows only a very weak signal of the existence of the cobalt element (Figure 6D). This confirms that the cobalt particles are largely embedded in the carbon phase so that only a small fraction of cobalt is XPS-detectable. In this sample, there are two subpeaks for the surface carbon species (Figure 6B). The strongest peak at 284.5 eV can be assigned to the graphene phase carbon as well as the adventitious hydrocarbon, and the peak at 285.6 eV is assigned to a small amount of CO_3^{2-} anions from the atmospheric CO_2.[28−30] The peak of O 1s photoelectrons is very weak, indicating that there is only little surface oxygen-containing species (Figure 6C). There are three subpeaks at 533.9, 532.6, and 531.4 eV, respectively. The first peak can be assigned to the oxygen in adsorbed water molecules and the second to the oxygen of the CO_3^{2-} anions.[28−30] The last peak is commonly known to arise from the oxygen in hydroxide ions, which suggests the existence of cobalt hydroxide on the surface. This is confirmed by the Co 2p photoelectron spectrum of the same sample (Figure 6D). The spectrum is noisy but shows the typical well-separated branches of $2p_{2/3}$ and $2p_{1/2}$ with a separation of about 15 eV in binding energy.[1−3] The peak with a binding energy of 778.6 eV and its corresponding $2p_{1/2}$ branch at 793.6 eV are assigned to elemental cobalt, which is the bulk species of the Co element as suggested by XRD results. The $2p_{3/2}$ peak with a binding energy of 780.9 eV and its $2p_{1/2}$ counterpart indicate that there are cobalt ions associated with hydroxide ions (Co−OH). The peaks at 783.1 and 798.1 eV can be assigned to the Co cations in association with carbonate ions (Co−CO_3). The existence of Co−OH and Co−CO_3 species is due to the exposure of the sample to air (containing CO_2 and H_2O) during sample handling after the synthesis.[28−30] As the XPS technique is surface sensitive, this observation reveals that the cobalt nanoparticles are in fact embedded underneath the graphene carbon so that only a small fraction of cobalt was

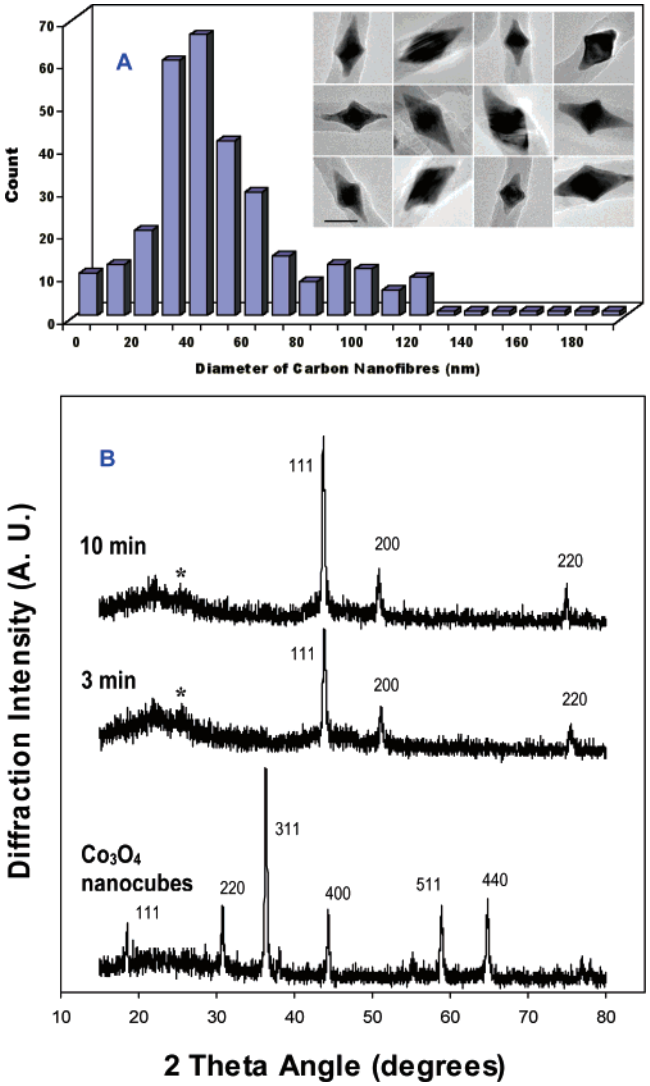

Figure 5. (A) Diameter distribution of the carbon nanofibers (the inset gives representative carbon tubules together with their central Co crystallites used in this statistic study; scale bar 50 nm). (B) XRD patterns of Co_3O_4 nanocubes and the formed fcc Co crystallites after 3 and 10 min of CVD reactions at 450 °C (C_2H_2 flow rate 10 mL/min). The asterisks in the XRD patterns (3 and 10 min) denote the graphene carbon phase formed on the two sides of a single-crystal Co center.

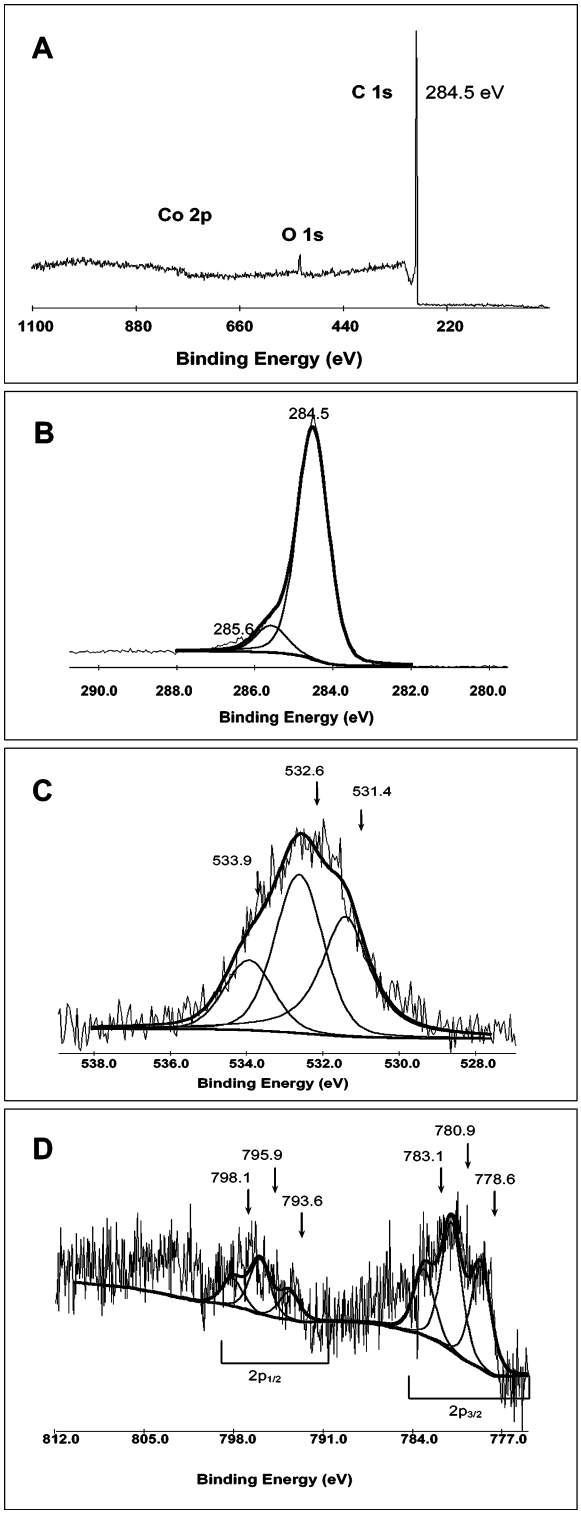

Figure 6. X-ray photoelectron spectra of the carbon composite material synthesized in this approach: (A) a wide scan; (B) 1s photoelectrons of carbon; (C) 1s photoelectrons of oxygen; (D) 2p photoelectrons of cobalt. The sample was prepared at 500 °C (10 min; C_2H_2 flow rate 10 mL/min).

detectable by XPS. Indeed, our TEM observation reveals that several layers of graphene were also deposited on the base of the biconical cobalt catalyst, where the entrance points of carbon are supposed to be. The TEM images in Figure 7 provide some detailed views on graphene structures formed on the utmost surface of the cobalt catalyst. A number of graphene layers were still formed on the central part of the cobalt catalyst (corresponding to the diameter of the carbon nanofiber). Although the X-ray of XPS can penetrate through these graphene layers to reach underneath cobalt, its (X-ray) intensity and the resultant intensity of photoelectrons of Co 2p had been significantly attenuated.

To investigate temperature effect, the as-prepared metal−carbon composite sample was heated inside an argon atmosphere (gas flow rate 10 mL/min) with a quartz-tubular furnace at 10 °C/min to 900 °C, and the temperature was held constant for 1 h. After this heat treatment, the sample was cooled to room temperature under ambient conditions within the same argon atmosphere. Interestingly, both the carbon and metal particles in the carbon nanofibers underwent significant reconstructions, as shown in Figure 8A and B. The lattice fringes of the graphene phase clearly show that the conical graphene layer stacks are now all changed to continuous parallel multiwalled carbon nanotubes (Figure 8A), during which the original discontinuous graphene layers were repaired by carbon diffusion and recrystallization. In Figure 8B, the metal nanoparticle is elongated along the internal cavity of the normal multiwalled carbon nanotubes. In particular, the two ends of the biconical cobalt

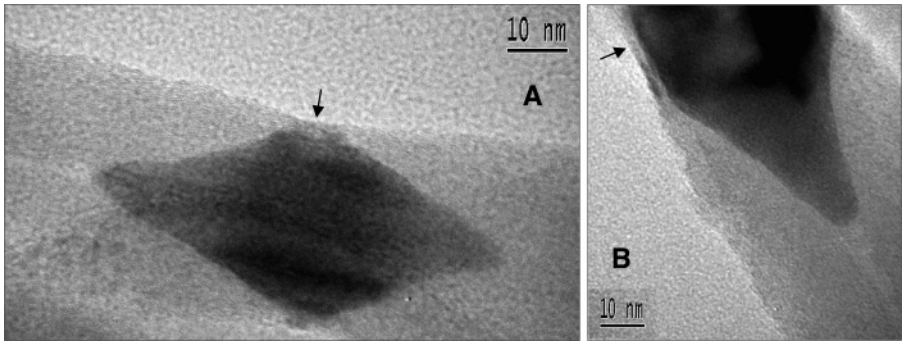

Figure 7. TEM images of the graphene-layer-covered Co nanocrystallite center. The arrows indicate the graphene layers on the Co nanocrystallite center.

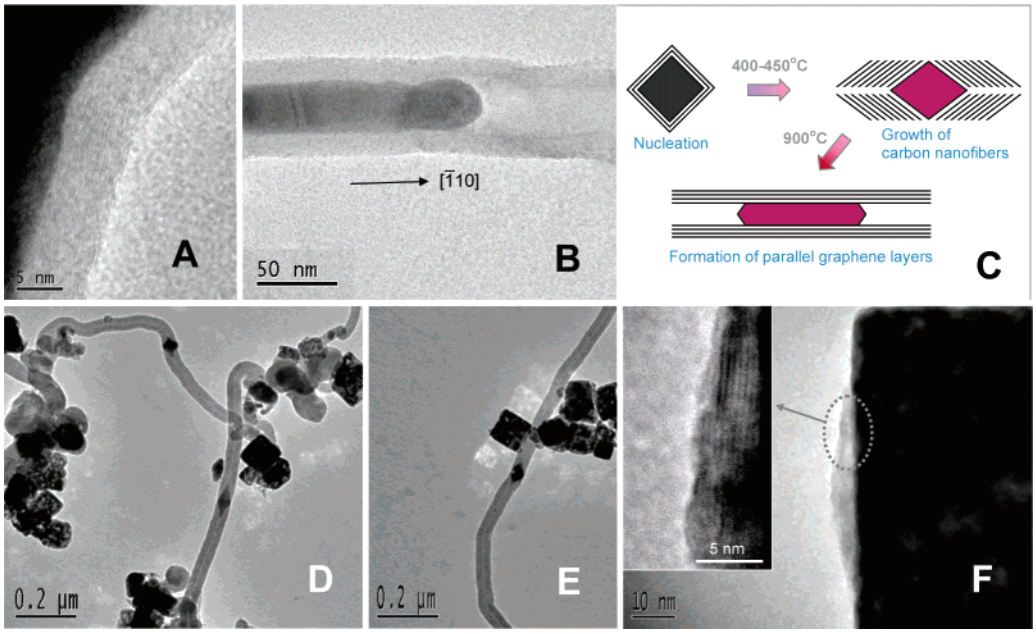

Figure 8. (A and B) Annealing of as-prepared cobalt-containing nanofibers (in an argon atmosphere, 900 °C, 1 h). (C) An observed mechanism for the formation of parallel graphene layers (initial Co/Co_3O_4 cube in black, fcc Co in purple, and graphene layers in black lines). (D and E) Competitive reduction for different sizes of Co_3O_4 nanocubes at a lower flow rate of C_2H_2 (5 mL/min; 10 min at 450 °C). (F) Graphene layers formed on the {100} surfaces of large Co_3O_4 nanocubes (C_2H_2 flow rate 5 mL/min; 10 min at 400 °C).

are no longer pointed but rounded with the atomically compact {111} facets. Once again, the SAED investigation (not shown) indicates that the confined cobalt nanorod is still single-crystalline, maintaining the same propagating orientations (i.e., ⟨110⟩ directions) as those in unannealed samples. Figure 8C gives a schematic illustration for the above process. The above investigation also suggests that extra precautions must be taken when interpreting a CVD mechanism, since the original shape of the metal catalyst and its actual growth interface might not be necessarily preserved at a reported nominal temperature due to additional reconstructions.

The reactions between Co_3O_4 nanocubes and C_2H_2 (flow rate 10 mL/min) were quite fast (Figure 5B). By decreasing the flow rate of C_2H_2 down to 5 mL/min, nevertheless, the reduction rate of the spinel oxide could be greatly lowered at the same temperature of 450 °C (Figure 8D and E). Under these less kinetically favorable conditions, some carbon nanofibers containing small cobalt nanocrystallites could still be formed but larger particles would just retain their pristine cubic morphology, though they had been partially etched (Co_3O_4 to Co) by the gaseous reducing agent acetylene. Compared to smaller particles, the large Co_3O_4 nanocubes are less reactive and were not able to compete with their smaller counterparts for the limited C_2H_2 supply. At as low as 400 °C, however, the large Co_3O_4 nanocubes were readily covered with a few graphene layers (Figure 8F), although they were only partially reduced (confirmed with XRD). The reactions in this low-temperature environment in fact shed light on the initial state of Co_3O_4 nanocube reduction and related conversion to metal cobalt. Upon the partial reduction in C_2H_2 (i.e., initial nucleation of graphene layers), indeed, the Co/Co_3O_4 solid mixture still keeps an overall cubic structure (Figure 8D−F). With the more favorable reacting conditions (higher flow rate of C_2H_2 and/or higher temperatures), all graphene-covered cubical solid mixtures would then be reshaped into the biconical cobalt core. As have been seen in Figures 2 and 3, the graphene layers wrapped on a reduced Co/Co_3O_4 nanocube would exert a force onto it due to the strong tendency of tubular formation (Figure 8C), inducing the elongation along the ⟨110⟩ directions of cobalt and subsequent growth of nanofibers.

Conclusions

In summary, we have demonstrated that the original shape, size, and symmetry (crystal orientation) of metal-oxide catalysts play paramount roles in determining a nominal formation mode of carbon nanofibers under hydrocarbon-CVD conditions. With our preshaped discrete metal-oxide nanocubes, a 2-fold sym-

metrical reconstructing metal catalyst is attained throughout the course of carbon deposition, revealing a bilateral base growth mode. In the same analogy, the synthetic approach with preshaped model catalysts may also be extendable to other mechanistic investigations on the reactivity of nanoparticles, general catalyst-assisted material synthesis, and intercalation chemistry. In principle, other metal−carbon nanocomposites with a complex branching morphology should also be attainable in the future when multiple-branched metallic catalysts can be prepared.

Acknowledgment. The authors gratefully acknowledge the financial support of the Ministry of Education, Singapore

Supporting Information Available: TEM images of as-prepared Co_3O_4 nanocubes, EDX spectrum of Co-containing nanocarbons, and the size statistics of nanocubes. This material is available free of charge via the Internet at http://pubs.acs.org.

References and Notes

(1) (a) Iijima, S. *Nature* **1991**, *354*, 56−58. (b) Ebbesen, T. W.; Ajayan, P. M. *Nature* **1992**, *358*, 220−222.

(2) Audier, M.; Oberlin, A.; Coulon, M. *J. Cryst. Growth* **1982**, *57*, 524−534.

(3) Charlier, J.-C.; De Vita, A.; Blase, X.; Car, R. *Science* **1997**, *275*, 647−649.

(4) Odom, T. W.; Huang, J.-L.; Kim, P.; Lieber, C. M. *J. Phys. Chem. B* **2000**, *104*, 2794−2809.

(5) Zheng, Q.; Jiang, Q. *Phys. Rev. Lett.* **2002**, *88*, 045503.

(6) Fan, S.; Chapline, M. G.; Franklin, N. R.; Tombler, T. W.; Cassell, A. M.; Dai, H. *Science* **1999**, *283*, 512−514.

(7) Gavillet, J.; Loiseau, A.; Journet, C.; Willaime, F.; Ducastelle, F.; Charlier, J.-C. *Phys. Rev. Lett.* **2001**, *87*, 275504.

(8) Gavillet, J.; Loiseau, A.; Ducastelle, F.; Thair, S.; Bernier, P.; Stéphan, O.; Thibault, J.; Charlier, J.-C. *Carbon* **2002**, *40*, 1649−1663.

(9) Hata, K.; Futaba, D. N.; Mizuno, K.; Namai, T.; Yumura, M.; Iijima, S. *Science* **2004**, *306*, 1362−1364.

(10) Rodriguez, N. M.; Chambers, A.; Baker, R. T. K. *Langmuir* **1995**, *11*, 3862−3866.

(11) Chambers, A.; Rodriguez, N. M.; Baker, R. T. K. *J. Phys. Chem.* **1996**, *100*, 4229−4236.

(12) Okai, M.; Muneyoshi, T.; Yaguchi, T.; Sasaki, S. *Appl. Phys. Lett.* **2000** *77*, 3468−3470.

(13) Helveg, S.; López-Cartes, C.; Sehested, J.; Hansen, P. L.; Clausen, B. S.; Rostrup-Nielsen, J. R.; Abild-Pedersen, F.; Nørskov, J. K. *Nature* **2004**, *427*, 426−429.

(14) Ngo, Q.; Cruden, B. A.; Cassell, A. M.; Sims, G.; Meyyappan, M.; Li, J.; Yang, C. Y. *Nano Lett.* **2004**, *4*, 2403−2407.

(15) Tanaka, A.; Yoon, S.-H.; Mochida, I. *Carbon* **2004**, *42*, 1291−1298.

(16) Andriotis, A. N.; Menon, M.; Froudakis, G. *Phys. Rev. Lett.* **2000**, *85*, 3193−3196.

(17) Mann, D. J.; Halls, M. D.; Hase, W. L. *J. Phys. Chem. B* **2002**, *106*, 12418−12425.

(18) Tsai, C. L.; Hsu, J. H.; Chen, C. F. *Appl. Phys. Lett.* **2003**, *82*, 4337−4339.

(19) Xu, R.; Zeng, H. C. *J. Phys. Chem. B* **2003**, *107*, 926−930.

(20) Feng, J.; Zeng, H. C. *Chem. Mater.* **2003**, *15*, 2829−2835.

(21) Lou, X. W.; Zeng, H. C. *J. Am. Chem. Soc.* **2003**, *125*, 2697−2704.

(22) Liu, B.; Zeng, H. C. *J. Am. Chem. Soc.* **2004**, *126*, 8124−8125.

(23) Yang, H. G.; Zeng, H. C. *Angew. Chem., Int. Ed.* **2004**, *43*, 5930−5933.

(24) Liu, B.; Zeng, H. C. *J. Am. Chem. Soc.* **2004**, *126*, 16744−16746.

(25) Yang, H. G.; Zeng, H. C. *J. Am. Chem. Soc.* **2005**, *127*, 270−278.

(26) Germain, V.; Li, J.; Ingert, D.; Wang, Z. L.; Pileni, M. P. *J. Phys. Chem. B* **2003**, *107*, 8717−8720.

(27) Dinega, D. P.; Bawendi, M. G. *Angew. Chem., Int. Ed.* **1999**, *38*, 1788−1791.

(28) Sampanthar, J. T.; Zeng, H. C. *Chem. Mater.* **2001**, *13*, 4722−4730.

(29) Xu, R.; Zeng, H. C. *Chem. Mater.* **2003**, *15*, 2040−2048.

(30) Xu, R.; Zeng, H. C. *Langmuir* **2004**, *20*, 9780−9790.